Nanotechnology, Science and Applications

Dovepress
Taylor & Francis Group

Open Access Full Text Article

ORIGINAL RESEARCH

Study of a Flexible ZnO/MWCNTs Thin Film Sensor for Hydrogen Peroxide Vapor Detection by Impedance Spectroscopy

Gohar Shahnazaryan[1], Artak Sayunts[1], Gevorg Shahkhatuni[1], Rima Papovyan[1], Zarine Simonyan[1], Gabriel Gevorgyan[1], Andranik Grigoryan[1], Dušan Kopecký[2], Mikayel Aleksanyan[1]

[1]Center of Materials Science and Nanotechnologies (Institute of Physics), Yerevan State University, Yerevan, Armenia; [2]Department of Mathematics, Informatics and Cybernetics, Faculty of Chemical Engineering, University of Chemistry and Technology Prague, Prague, Czech Republic

Correspondence: Artak Sayunts, Center of Materials Science and Nanotechnologies (Institute of Physics), Yerevan State University, 1 Alex Manoogian, Yerevan, 0025, Armenia, Email sayuntsartak@ysu.am

Introduction: The growing demand for sensors capable of detecting hydrogen peroxide vapor (HPV) in industrial and medical applications has led to increased research activity in this field. Despite significant progress, there remains a strong need for the development of new HPV-sensitive materials as well as for improving the performance of existing sensor systems. This work presents a flexible hydrogen peroxide vapor sensor employing a ZnO/MWCNTs (multi-walled carbon nanotubes) thin film as the sensing layer and provides a detailed impedance-based analysis.

Methods: The frequency dependence of the real and imaginary components of the complex impedance was measured in air and under exposure to HPV at operating temperatures ranging from room temperature to 200 °C. The influence of ultraviolet (UV) irradiation on the impedance response of the ZnO/MWCNTs sensor was also examined. The structural, morphological, and compositional characteristics of the ZnO/MWCNTs composite were analyzed by scanning electron microscopy (SEM), transmission electron microscopy (TEM), energy-dispersive X-ray spectroscopy (EDS), and X-ray photoelectron spectroscopy (XPS).

Results: Analysis of the impedance spectra enabled the proposal of an equivalent electrical circuit describing the sensor structure. The parameters of the circuit elements were determined, and the calculated impedance curves showed good agreement with the experimental data. A linear increase in sensor sensitivity was observed with increasing temperature up to 175 °C. Ultraviolet (UV) irradiation resulted in an approximately twofold enhancement of sensor sensitivity at room temperature.

Conclusion: It was demonstrated that the flexible polyimide substrate with platinum interdigitated electrodes makes a significant contribution to the overall impedance of the ZnO/MWCNTs sensor structure. In the equivalent circuit, this contribution is represented by a parallel parasitic capacitance ($C_0 \approx 1.67 \times 10^{-11}$ F). Exposure to hydrogen peroxide vapor mainly affects the resistance of the ZnO/MWCNTs sensing film. The validity of the proposed equivalent electrical circuit is confirmed by the close correspondence between the calculated Nyquist plots and the experimental impedance data.

Keywords: flexible sensor, impedance spectroscopy, equivalent circuit, zinc oxide, multi-walled carbon nanotubes, hydrogen peroxide vapor

Introduction

Impedance spectroscopy is one of the most informative methods for studying semiconductor-based sensor structures. It involves analyzing the system response to a small-amplitude sinusoidal excitation signal.[1,2] Investigating the frequency dependencies of the real and imaginary components of the complex impedance provides insight into the factors and processes responsible for gas sensitivity, enables a quantitative assessment of the contributions of individual components of the sensor structure, and allows the extraction of parameters characterizing the gas-sensitive film.

https://doi.org/10.2147/NSA.S577983
Received: 3 November 2025
Accepted: 17 February 2026
Published: 6 March 2026

Impedance analysis typically requires selecting or constructing an equivalent electrical circuit that adequately reflects the electrical and chemical processes occurring within the system, determining the parameters of the resistive and capacitive elements of the circuit, and calculating the fitting frequency-dependent impedance curves. It is worth noting that impedance spectroscopy is not a new method; it has been employed since the 1940s, primarily for analyzing electrochemical systems.[1,3,4] However, its adoption in sensor research has been limited due to certain challenges, such as the difficulty in selecting an appropriate equivalent circuit and the need for additional measurement data. In recent decades, advancements in software tools have significantly reduced the time required for processing experimental data, which has contributed to the growing popularity of impedance spectroscopy.[5–12]

Sensors for hydrogen peroxide (H_2O_2) detection are widely applied in various industrial sectors, including food, textile, paper, and pharmaceutical industries, as well as in the production of cleaning and disinfecting agents, environmental monitoring, analytical chemistry, and safety systems. Since H_2O_2 is a substance with a defined permissible exposure limit, exceeding which poses a risk to human health, research focused on its detection and concentration assessment in ambient air remains highly relevant.[13–15]In particular, sensors for HPV detection are of significant interest in clinical diagnostics for rapid and reliable disease identification and for monitoring treatment progress. Elevated concentrations of hydrogen peroxide in exhaled breath have been associated with bronchial asthma and chronic obstructive pulmonary disease, making HPV sensors promising components for noninvasive pulmonary diagnostics.

Among the various types of HPV sensors developed to date, including electrochemical, amperometric, and colorimetric devices, semiconductor metal oxide-based sensors occupy a special position due to their simple fabrication processes and low production cost.[16–19] Research in this field remains highly relevant, as many important performance parameters of existing sensors still require improvement. Current efforts focus on the selection of suitable dopants and their optimal concentrations, optimization of oxide microstructure through improved fabrication conditions, and deeper understanding of gas-sensing mechanisms. In parallel, the search for new gas-sensitive materials and the development of advanced fabrication technologies continue, with nanotechnology playing a key role in these advances.

In this work, a composite ZnO/MWCNTs structure is employed as the HPV-sensitive element of the sensor. The novelty of this work lies in combining a ZnO/MWCNTs composite with impedance spectroscopy for HPV in a flexible sensor platform. This approach enables characterization of the sensor response beyond conventional resistive methods and has not been previously reported for this material. ZnO is a well-known n-type semiconductor featuring a direct band gap of ~3.37 eV and a hexagonal wurtzite lattice ($a \approx 3.25$ Å, $c \approx 5.21$ Å). With a wide band gap and an exciton binding energy near 60 meV, ZnO shows pronounced surface-controlled conductivity, where chemisorbed and ionized oxygen species significantly influence its electrical behavior.[20] MWCNTs, on the other hand, offer excellent electrical conductivity and extremely high surface area, acting as efficient charge-transport channels with plentiful active sites. When ZnO nanostructures are coupled with MWCNTs networks, numerous oxide-carbon junctions are formed facilitating rapid electron transfer. This composite structure enhances gas-induced resistance changes, while the tailored ZnO morphology further improves sensitivity and response-recovery speed, yielding an efficient resistive sensing film.[21] ZnO/MWCNTs composites are well suited for flexible sensors due to the synergistic combination of the mechanical flexibility and electrical conductivity of MWCNTs with the chemical sensitivity and stability of ZnO. This synergy enables reliable charge transport and sensing performance under mechanical deformation on flexible substrates.[22] Palladium nanoparticles were added to improve the catalytic properties of the ZnO/MWCNTs composite. Pd acts as a chemical reaction activator, providing additional active sites on the surface and facilitating charge transfer within the composite. This catalytic effect enhances the sensitivity and speed of the sensor toward HPV.[23]

The aim of this work was to fabricate a flexible HPV sensor based on a ZnO/MWCNTs thin film and to investigate its sensing properties using impedance spectroscopy.

Experimental Setup and Measurement Procedure

The zinc oxide sputtering target was prepared using commercially available ZnO nanopowder (particle size 20–40 nm, purity 99.9%). The powder was homogenized by prolonged milling and mixing for 20 h to ensure uniformity, followed by pre-drying at 350 °C for 8 h to remove residual moisture and volatile species before target fabrication. Afterward, it was compacted into a disk-shaped pellet (50 ×4 mm) and subjected to thermal treatment at 1250 °C for 30 h to ensure

densification. The obtained ceramic target underwent subsequent mechanical and chemical finishing. For film deposition, the target was mounted into the RF magnetron sputtering unit at a distance of 12 cm from the substrate holder. The system was initially evacuated to a base pressure of ~1×10^{-4}. During deposition, the chamber pressure was stabilized at ~1×10^{-3} using high-purity argon supplied at a flow rate of 30 SCCM. The sputtering was performed at a power of 70 W for 25 min, resulting in a film with a thickness of ~100 nm. Accelerated argon ions bombarded the ZnO target surface, ejecting ZnO nanoparticles, which traveled through the vacuum and condensed on the heated (100 °C) polyimide substrate, forming a granular thin-film layer.

To further enhance the sensing layer, MWCNTs were introduced. The nanotubes were pre-pressed into a small pellet (4 × 3 mm) and employed as a secondary sputtering target. MWCNTs were deposited onto the ZnO-coated substrates in the form of nanoscale clusters using e-beam deposition. The chamber was pumped to a base pressure of 2×10^{-3} and the working pressure during deposition was maintained at 7.5×10^{-2}. The electron beam was operated at an accelerating voltage of 0.5 kV. The deposition time was 2 min, while the substrate temperature was maintained at 150 °C and the target–substrate distance was set to 7 cm. This approach ensured uniform cluster formation and good adhesion of the MWCNTs onto the ZnO layer. Finally, the composite film was sensitized with palladium nanoparticles deposited via DC magnetron sputtering. The complete sensor structure was annealed at 200 °C for 3 h to stabilize its morphology and improve gas-sensing activity. Figure 1a and b illustrate the fabrication steps of the ZnO/MWCNTs sensitive film. Figure 2a and b present the real photo (a) and the corresponding illustration (b) of the sensor structure. The active sensing area measured 8.2×5.15 mm, with an inter-electrode gap of 0.45 mm and total sensor dimensions of 10×12 mm.

These films served as the active sensing elements of the sensor in subsequent impedance spectroscopy and gas-sensing experiments. The block diagram of the system used to measure the impedance characteristics of the fabricated ZnO/MWCNTs sensor was presented in our earlier work.[12] The laboratory setup combined capabilities for studying sensors under varying operating temperatures, controlled gas environments, and exposure to ultraviolet (UV) irradiation.

The sensor was placed on a dedicated platform inside a hermetically sealed experimental chamber. The impedance measurements of the sensor structure were carried out using a Potentiostat/Galvanostat/EIS system (Wonatech Zive SP1) over a frequency range from 10^{-1} Hz to 10^{6} Hz. Measurements were performed under a 1 V bias voltage, superimposed with a sinusoidal signal of 100 mV amplitude. The impedance data were recorded using the Smart Manager 6 software provided with the Zive SP1 instrument. The experimental measurements were performed both in air and in the presence of HPV at a concentration of 100 ppm. To create the target gas atmosphere, after thermal stabilization of the system at the specified temperature, a pre-calculated amount of aqueous hydrogen peroxide solution was introduced into the

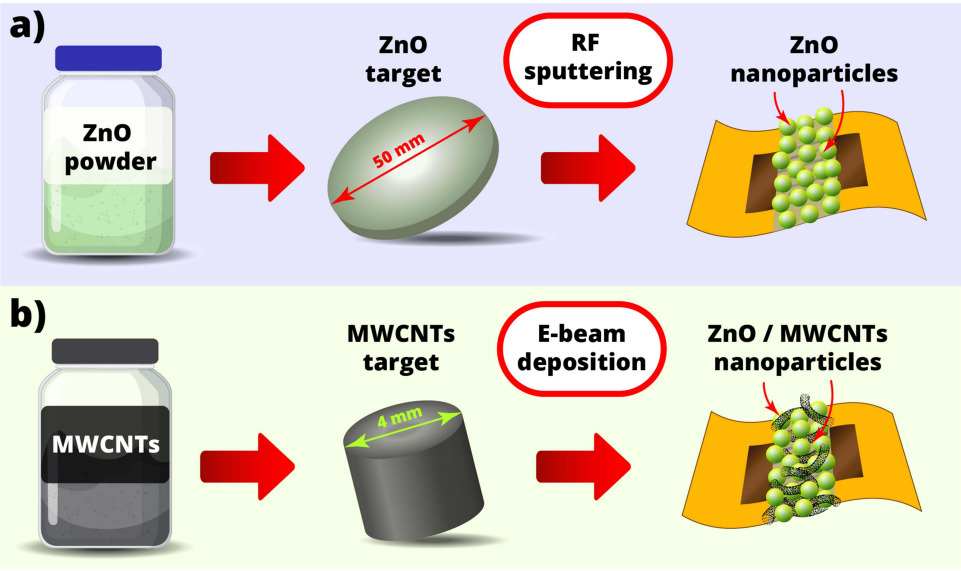

Figure 1 Fabrication process of the ZnO (**a**) and ZnO/MWCNTs (**b**) films.

https://doi.org/10.2147/NSA.S577983

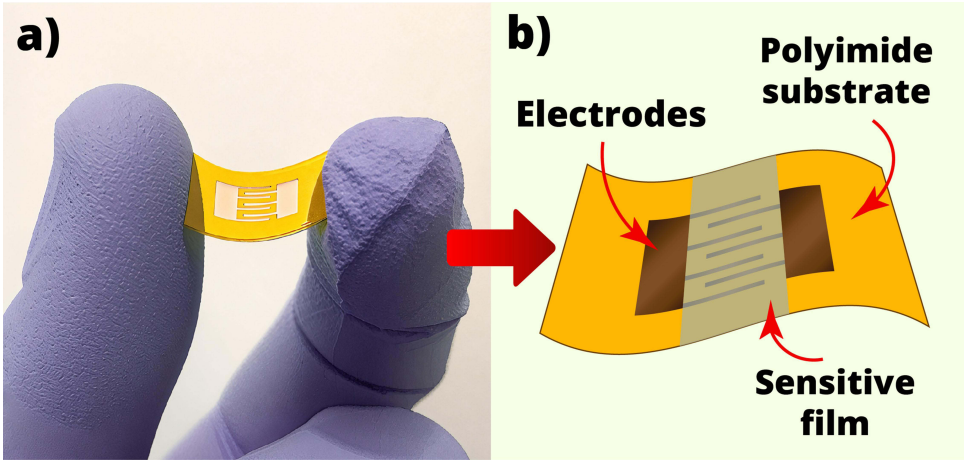

Figure 2 The real photo (**a**) and illustration (**b**) of the fabricated sensor structure.

experimental chamber, resulting in a vapor concentration with a precision of ±1.5%.[24] Upon contact with the heated platform (maintained at 100 °C), the liquid phase was converted into vapor. Impedance measurements of the ZnO/MWCNTs sensor were conducted over an operating temperature range from room temperature to 200 °C. Heating was achieved by applying the required voltage to the heater using the KEITHLEY 2231A-30-3 power supply. Before each measurement, the sample was thermally stabilized for 30 minutes at the operating temperature. The temperature deviation during measurement did not exceed ±1 °C. To examine the influence of UV irradiation on the impedance behavior, a UV light-emitting diode (LED – RC35E6-UIE-AR) was placed 1 cm from the sensor inside the measurement chamber, providing intense illumination with a wavelength of 365 nm. The ZnO/MWCNTs composite was characterized by SEM and TEM analysis to evaluate its morphological and structural features at different length scales, respectively. EDS and XPS were employed to identify the elemental composition and surface chemical states of the composite, respectively. The morphology of the ZnO/MWCNTs composite was analyzed by SEM (Mira 3 LMH, Tescan). TEM analysis of the MWCNTs was performed using a JEOL 2200 FS instrument. The elemental composition was determined using EDS (Quantax 200 with XFlash 6|10, Bruker), and the XPS survey spectrum was obtained with a K-Alpha system (Thermo Fisher Scientific, USA).

Results and Discussion

Characterization

The SEM images of the ZnO sample are presented in Figure 3a and b, showing uniformly distributed nanograins with an average size of approximately 50 nm and a crack-free morphology. The SEM images of the MWCNTs sample are shown in Figure 4a and b, exhibiting entangled tubular structures with smooth surfaces and on the order of tens of micrometers. Nanotubes of different diameters were fitted into large nanotubes, forming nanotube meshes.

Figure 5a and b show the TEM image of the MWCNTs revealing an average diameter of around 35 nm. In the TEM images of the MWCNTs, the contrast between light and dark regions is caused by differences in wall thickness and electron scattering. Dark regions are associated with thicker or overlapping nanotube walls, while lighter regions correspond to thinner walls or hollow cores, confirming the tubular structure of the MWCNTs.[25] The EDS spectrum of the ZnO and MWCNTs samples (Figure 6) shows clear elemental peaks corresponding to zinc and oxygen for ZnO material, and carbon for the MWCNTs. Silicon peaks arise from the underlying substrate.[26,27]

The XPS survey spectrum of the ZnO/MWCNTs composite (Figure 7a) confirmed the presence of zinc, oxygen, and carbon as the primary elements, consistent with the expected composition. High-resolution XPS spectra were recorded to analyze the chemical states of individual elements. The Zn 2p spectrum (Figure 7b) exhibited two characteristic peaks at approximately 1022.5 eV (Zn $2p_3/_2$) and 1045.5 eV (Zn $2p_1/_2$) energy points, indicating the presence of Zn^{2+} in the ZnO lattice. The O 1s spectrum (Figure 7c) showed a single peak at 531.2 eV, corresponding to lattice oxygen in ZnO. The

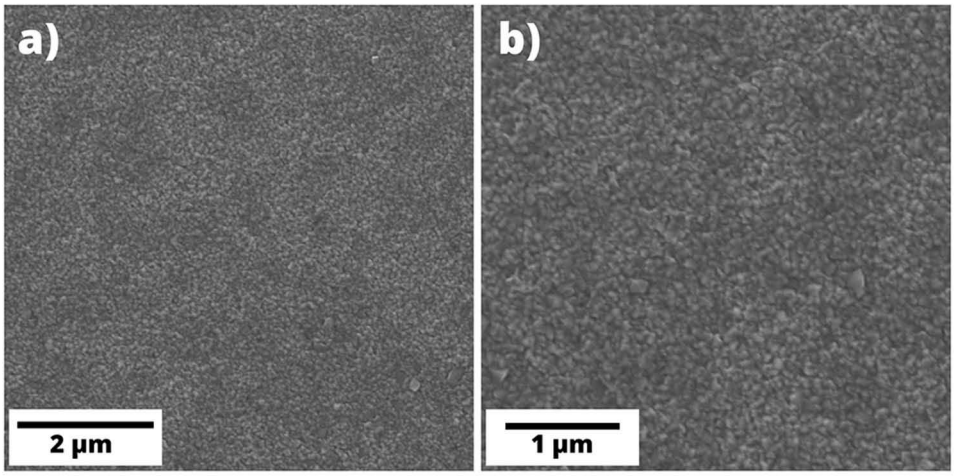

Figure 3 The SEM images of the ZnO film with 2 μm (**a**) and 1 μm (**b**) scalebars.

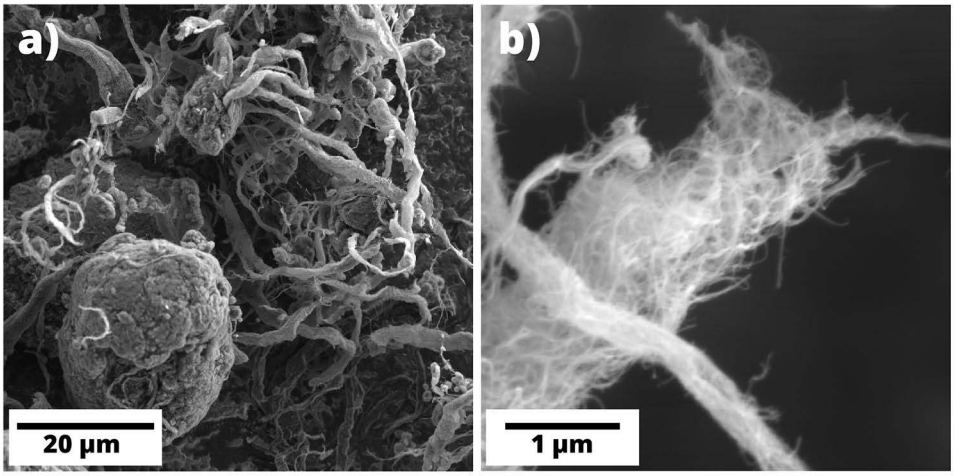

Figure 4 The SEM images of the MWCNTs material with 20 μm (**a**) and 1 μm (**b**) scalebars.

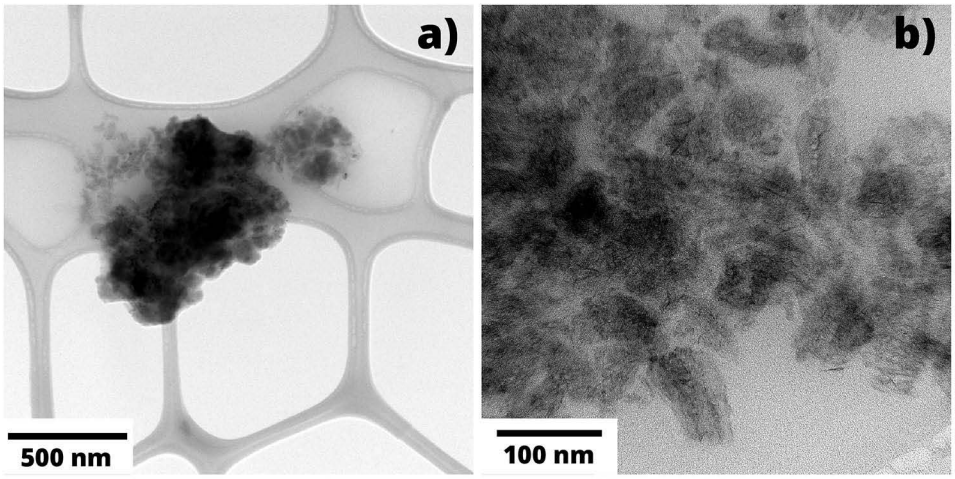

Figure 5 The TEM image of the MWCNTs material with 500nm (**a**) and 100 nm (**b**) scalebars.

https://doi.org/10.2147/NSA.S577983

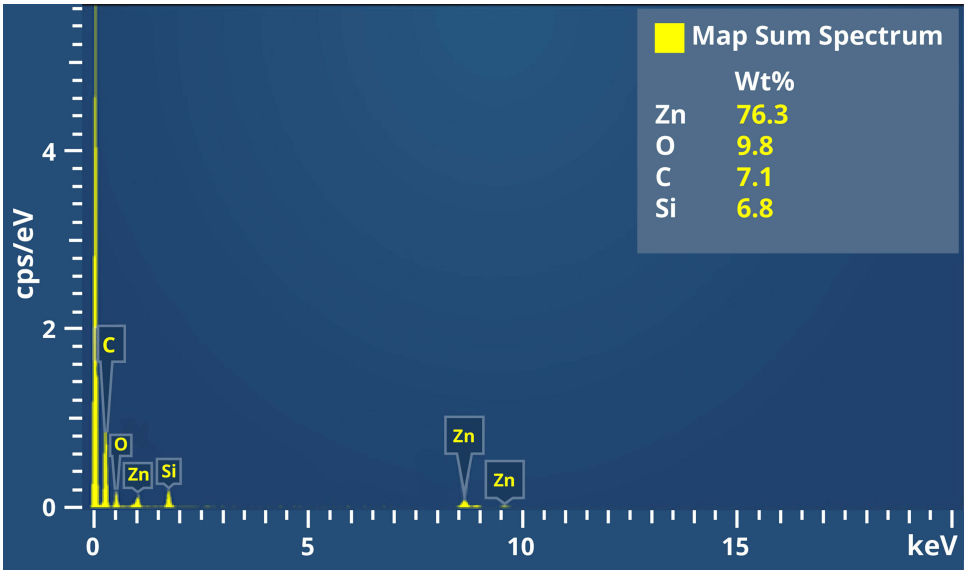

Figure 6 The EDS spectrum of the ZnO/MWCNTs material.

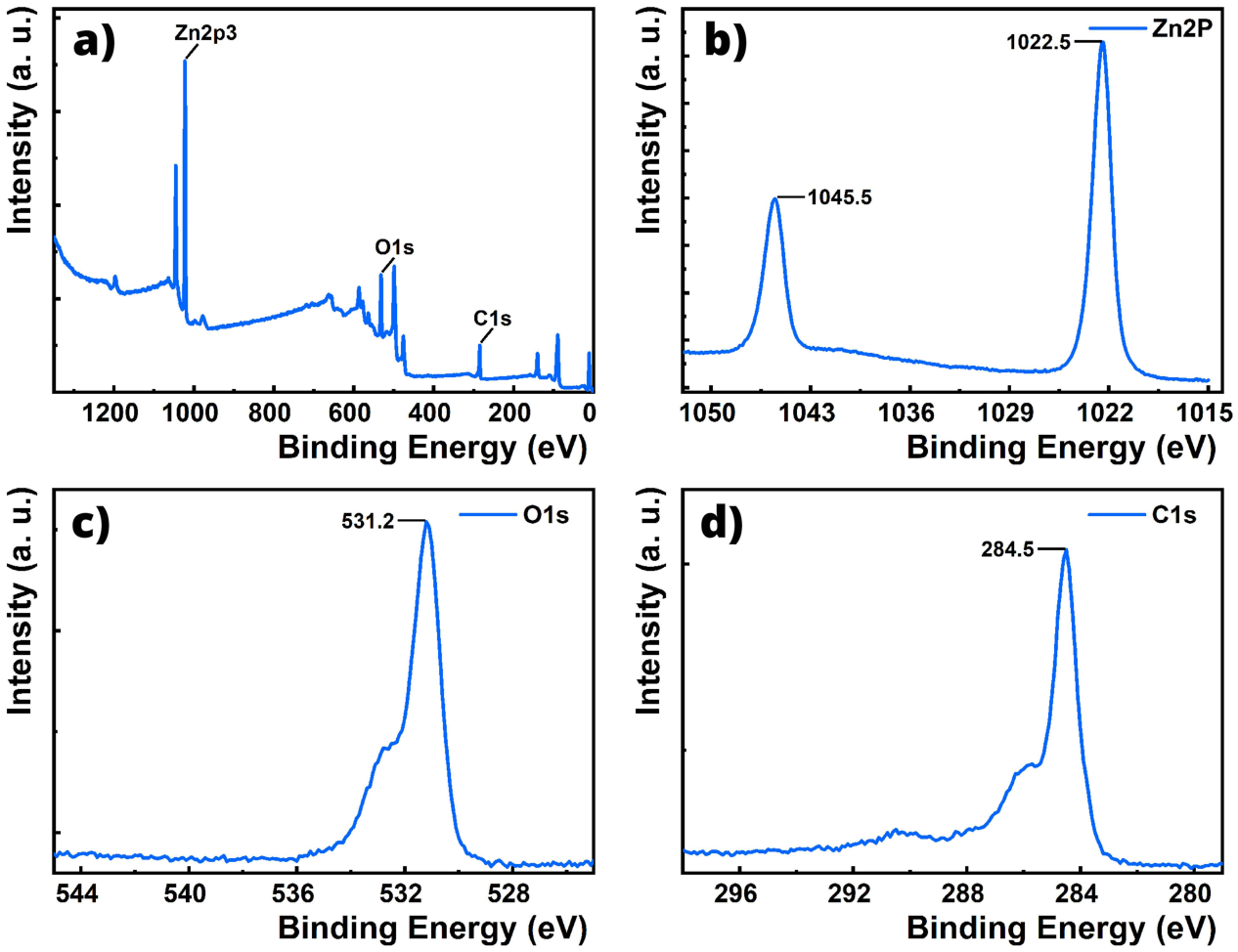

Figure 7 The XPS survey spectrum of the ZnO/MWCNTs material (**a**), and high-resolution spectra of Zn 2p (**b**), O 1s (**c**), and C 1s (**d**).

https://doi.org/10.2147/NSA.S577983

C 1s spectrum (Figure 7d) was dominated by a peak at 284.5 eV, corresponding to sp^2-hybridized carbon in the graphitic structure of the MWCNTs. In addition, a secondary component at 285.7 eV was observed, which was attributed to sp^2 (C=C) and sp^3 (C–C) carbon bonds associated with structural disorder and defect-related states within the MWCNTs framework. The O 1s spectrum shown a shoulder at 532.8 eV, which was assigned to surface-related oxygen species such as hydroxyl groups, adsorbed oxygen, and defect-associated non-lattice oxygen in ZnO.[27,28]

Impedance Measurements

One of the key structural elements of metal oxide sensors is the substrate, which serves as the base for depositing the gas-sensitive film using various techniques. The substrate should have minimal influence on the overall impedance of the sensor structure.[29] In this work, we used a flexible polyimide film as the substrate, on which platinum interdigitated electrodes were applied via ion-plasma sputtering. Besides, the geometry of the interdigitated electrodes might influence on the sensitivity of the sensor.[30] This substrate offers excellent dielectric properties, strong adhesion to the sensing layer, and high resistance to elevated temperatures and repeated thermal cycling. The influence of the substrate on the impedance characteristics of sensor structures is a factor repeatedly highlighted in studies employing impedance spectroscopy for gas sensor characterization.[2,12,31] This is due to the fact that the substrate, together with the various components (for example, a temperature sensor, a heater, contacts of different configurations, etc.) often has a significant effect on the sensor impedance. To address this consideration, the impedance characteristics of the substrate, comprising a flexible polyimide film with platinum interdigitated electrodes, were independently measured across a wide temperature range (from room temperature to 220 °C), under varying bias voltages (0 – 2 V) and the amplitude of the disturbing voltage (10 –300 mV). Representative data are presented in Figure 8a and b. The frequency dependence of both the real (Z'_{sub}) and imaginary (Z''_{sub}) components of the substrate complex impedance remained stable across all conditions tested.[32,33]

Throughout the entire investigated frequency range, the imaginary component of the impedance significantly exceeds the real component in absolute value. As a result, the modulus of the total impedance almost coincided with the imaginary component $Z = Z''_{sub.}$ At frequencies below 10 Hz, the values of both the real and imaginary components of the complex impedance of the substrate exceed 10^8 Ohm indicating that in the low-frequency region the substrate did not make a significant contribution to the complex impedance of the sensor structure. In the high-frequency region (above 100 Hz), the impedance characteristics of the substrate can be described by the expressions:

$$Z'_{sub} = R_c + a/\omega^{0.85} \; and \; Z''_{sub} = b/\omega \tag{1}$$

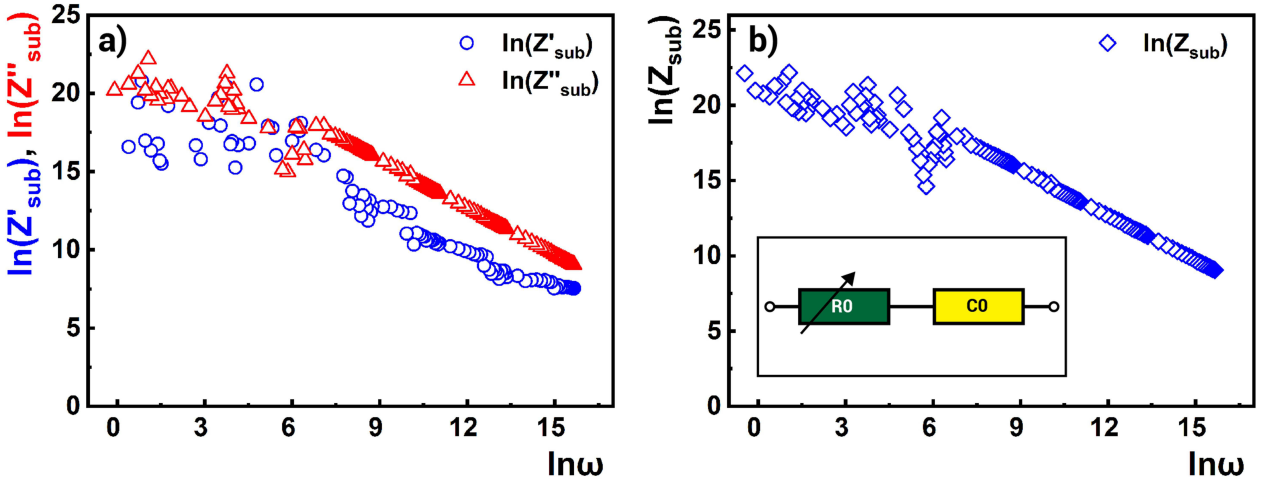

Figure 8 (**a**) Typical frequency dependences of the real (Z'_{sub}) and imaginary (Z''_{sub}) components of the complex impedance of a flexible polyimide substrate with platinum interdigitated electrodes. (**b**) Equivalent circuit and frequency dependencies of absolute value (Z_{sub}) complex impedance of the flexible polyimide substrate.

https://doi.org/10.2147/NSA.S577983

where ω is angular frequency, $R_c \sim 1.8\times10^3$ Ohm, $a \sim 5.7\times10^8$ and $b \sim 6\times10^{10}$. The constant resistance R_c maked a noticeable contribution to the real component of the impedance at frequencies above 10^5 Hz. This resistance was most likely associated with cable effects as well as inductive contributions from the experimental setup.[12] In subsequent measurements, these effects were eliminated through appropriate calibration. Thus, at frequencies above 100 Hz, the flexible polyimide substrate with interdigitated electrodes can be represented by an equivalent circuit consisting mainly of a variable resistance $R_0 = a/\omega^{0.85}$ ($a \sim 10^8 - 10^9$) connected in series with a constant capacitance $C_0 = 1/b \approx 1.67\times10^{-11}$ F. Therefore, it can be concluded that the flexible polyimide substrate with platinum interdigitated electrodes contributes to the complex impedance of the sensor primarily in the form of a "parasitic" capacitance C_0 during measurements at frequencies above 100 Hz.

The results of impedance measurements of the sensor structure in air at different operating temperatures are shown in Figure 9a as Nyquist plots. An increase in sensor heating temperature led to a decrease in the radius of the Nyquist semicircle. It is known that when modeling polycrystalline structures, the influence of both grain bulk and grain boundaries can be accounted for using an equivalent circuit consisting of two series-connected circuits, each comprising a resistor R and capacitor C in parallel, and characterized by a time constant equal to RC.[34] The presence of a single semicircle in the investigated sensor may indicate that the time constants of these two RC branches are of the same order of magnitude, resulting in overlapping contributions from processes occurring within the grain bulk and at grain boundaries.[6]

For the modeling of the sensor structure, the equivalent circuit depicted in Figure 9b was adopted. The element R represents the resistance of the gas-sensitive film, encompassing both bulk and grain boundary resistances. To account for the dispersion in grain boundary resistances and their associated capacitances, a constant phase element (CPE) was employed, whose impedance is defined by the following expression:

$$Z_{CPE} = A^{-1}(i\omega)^{-n} \tag{2}$$

where A is the proportionality factor, whose units depend on the power exponent n. It should be noted that the CPE does not have a strictly defined physical meaning and serves as a universal tool for modeling polycrystalline films.[2,31,35] Table 1 presents the parameters of the selected equivalent electrical circuit using the ZMAN 2.3 software.

The resistance R_{air} decreases significantly with increasing operating temperature, as shown in Figure 10a. It is known that oxygen vacancies in the polycrystalline zinc oxide film create shallow donor centers that are nearly fully ionized at room temperature. Therefore, the film resistance R_{air} is most likely determined by the height of potential barriers at grain boundaries. Increasing the sensor operating temperature probably activates a hopping conduction mechanism due to an

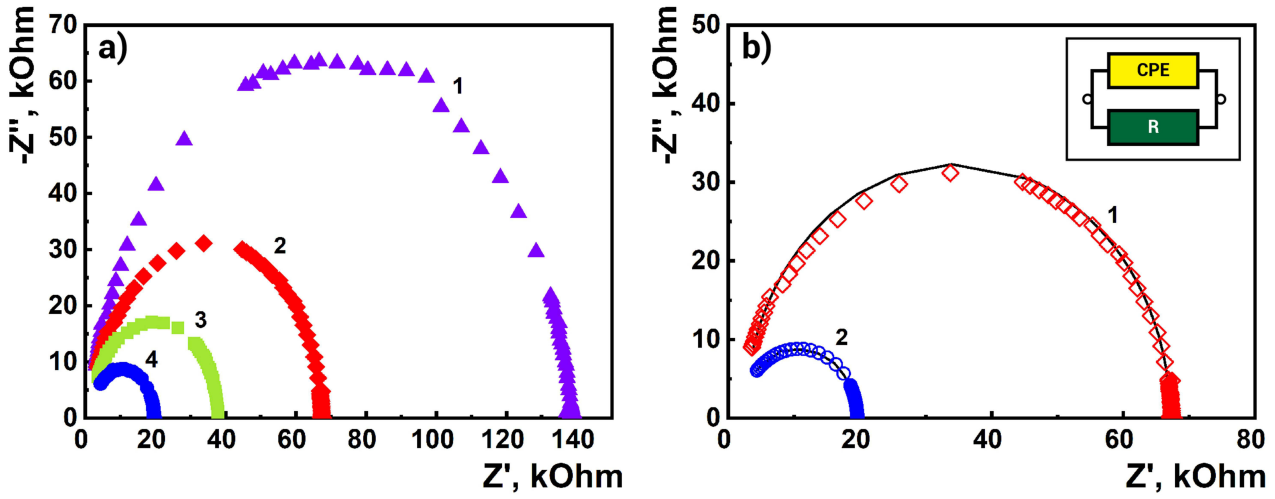

Figure 9 (**a**) Nyquist plots of the ZnO/MWCNTs sensor measured in air at operating temperatures of 25 °C (1), 75 °C (2), 125 °C (3), and 200 °C (4). (**b**) Equivalent electrical circuit proposed for the sensor structure and comparison between the obtained at 75 °C (1) and 200 °C (2) experimental data (dots) and theoretically calculated fitting curves (solid lines).

https://doi.org/10.2147/NSA.S577983

Table 1 Parameter Values of the Equivalent Electrical Circuit Modeling of the Sensor

Operating Temperature	Measurements in Air			Measurements in HPV Atmosphere		
T, °C	R_{air}, Ohm	$A\times10^{-11}$, F	*n*	R_{gas}, Ohm	$A\times10^{-11}$, F	*n*
25	136,053	2.88	0.964	705,742	2.36	0.982
50	74,235	3.62	0.934	548,481	2.11	0.976
75	65,191	2.33	0.98	491,425	2.35	0.974
100	49,719	3.85	0.938	484,714	2.2	0.971
125	35,840	2.38	0.99	393,658	2.34	0.966
175	20,360	2.44	0.972	260,865	2.31	0.964
200	17,736	2.47	0.993	155,581	3.12	0.957

increased number of electrons having sufficient energy to overcome the energy barrier between grains. Using the resistance values R_{air} obtained from the impedance analysis, the activation energy of the semiconductor film conductivity was determined. Based on the dependence of ln(1/R) = f(1/T), the energy corresponding to the barrier height between grains was calculated from the curve in Figure 10b to be approximately 0.134 eV. According to the data in Table 1, the exponent *n* remains close to unity regardless of temperature, which indicates that in this case the constant A characterizes the capacitance of a capacitor, with its value changing only slightly with temperature. For the investigated sensor, this capacitance arises not only from the gas-sensitive film, but its main contribution comes from the substrate capacitance, which, as established, is independent of temperature. The capacitance of the gas-sensitive film was not obtained in a "pure" form in the present work due to the contribution of the substrate capacitance. Our further studies will be focused on separating the capacitance of the sensing film from the total capacitance described by the parameter A.

Using the data from Table 1, the fitting impedance dependences were calculated and are presented in Figure 9b for comparison. It is evident that the good agreement between the experimental data and the theoretically calculated dependences confirms the reliability of the selected equivalent electrical circuit for describing the processes occurring in the fabricated sensor structure.

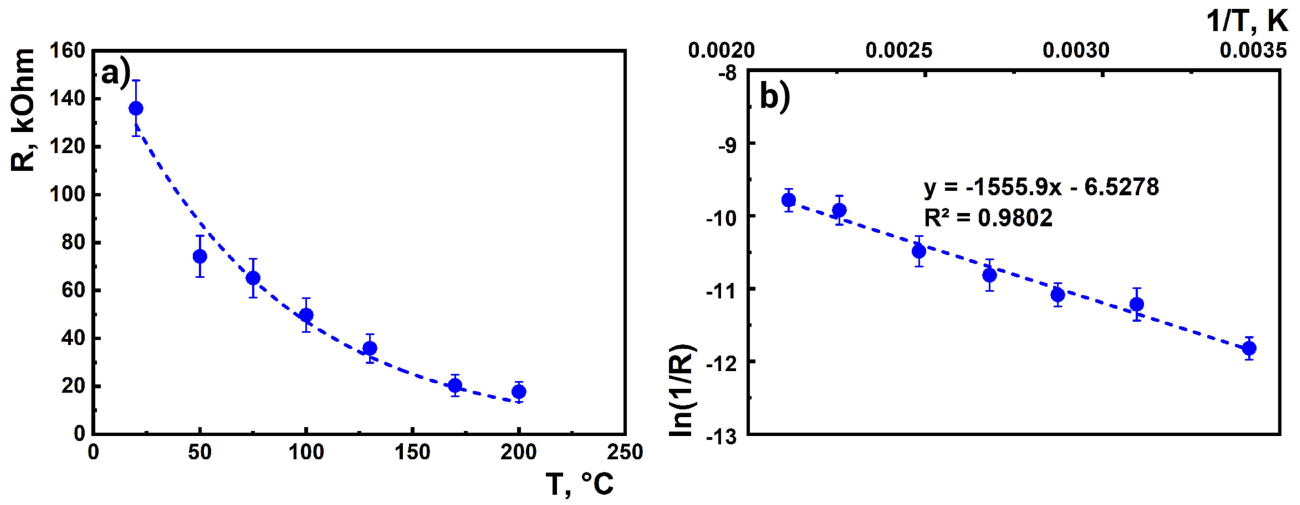

Figure 10 (**a**) Temperature dependence of the sensor resistance; (**b**) Determination of the activation energy of conductivity of the ZnO/MWCNTs film. The dashed lines represent the approximation curves, and the error bars indicate the deviations.

https://doi.org/10.2147/NSA.S577983

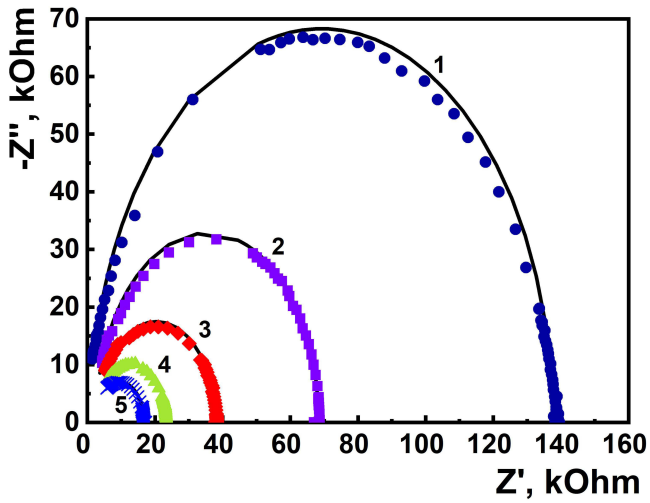

Figure 11 Nyquist plots of the ZnO/MWCNTs sensor obtained from measurements in air without UV irradiation at 25 °C (1) and under UV irradiation at 25 °C (2), 100 °C (3), 150 °C (4), and 200 °C (5). The experimental results are shown by dots, while the solid lines represent the theoretically calculated fitting dependences.

One of the commonly applied approaches for reducing sensor operating temperature and enhancing sensitivity is UV irradiation of the active sensor surface using modern low-power, portable light-emitting diode sources. UV illumination leads to a significant decrease in the resistance of the semiconductor film due to photogenerated charge carriers and simultaneously promotes chemical reactions at the gas-sensitive layer interface. As a result, UV activation can substantially enhance gas sensitivity, even at room temperature.

Figure 11 shows the results of impedance measurements of the sensor structure carried out in air under UV irradiation (for comparison, the Nyquist curve measured at room temperature without UV irradiation is also presented), along with the corresponding fitting dependences. UV irradiation likely leads to the generation of additional free carriers and, similar to the increase in temperature, provides carriers with sufficient energy to overcome the potential barrier between grains. As a result, the sensor resistance at room temperature decreases by almost a factor of three. The fitting curves were calculated using the equivalent circuit parameters listed in Table 2, which were determined with the ZMAN 2.3 software.

Figure 12a and b illustrates the transformation of the impedance characteristics of the sensor structure under exposure to HPV at a concentration of 100 ppm. Without altering the overall shape of the curve, the radius of the Nyquist semicircle increases sharply upon exposure to the target gas. According to the established gas–solid interaction mechanism.[12,36,37] H_2O_2 molecules undergo catalytic decomposition on the surface of the metal oxide sensing film, yielding water and oxygen species. The liberated oxygen molecules chemisorb onto the surface and extract electrons

Table 2 Parameters of the Equivalent Electrical Circuit Modeling for the Sensor Under UV Illumination

Operating Temperature	Measurements in Air Under UV Irradiation			Measurements in HPV Atmosphere Under UV Irradiation		
T, °C	R_{air}, Ohm	$A{\times}10^{-11}$, F	*n*	R_{gas}, Ohm	$A{\times}10^{-11}$, F	*n*
25	65,774	1,89	0.985	626,341	2.42	0.981
100	35,477	2.11	0.981	241,564	2,46	0,98
150	20,653	2.15	0.988	160,806	2,89	0,952
200	14,774	3,59	0.96	132,886	2,84	0.957

 https://doi.org/10.2147/NSA.S577983

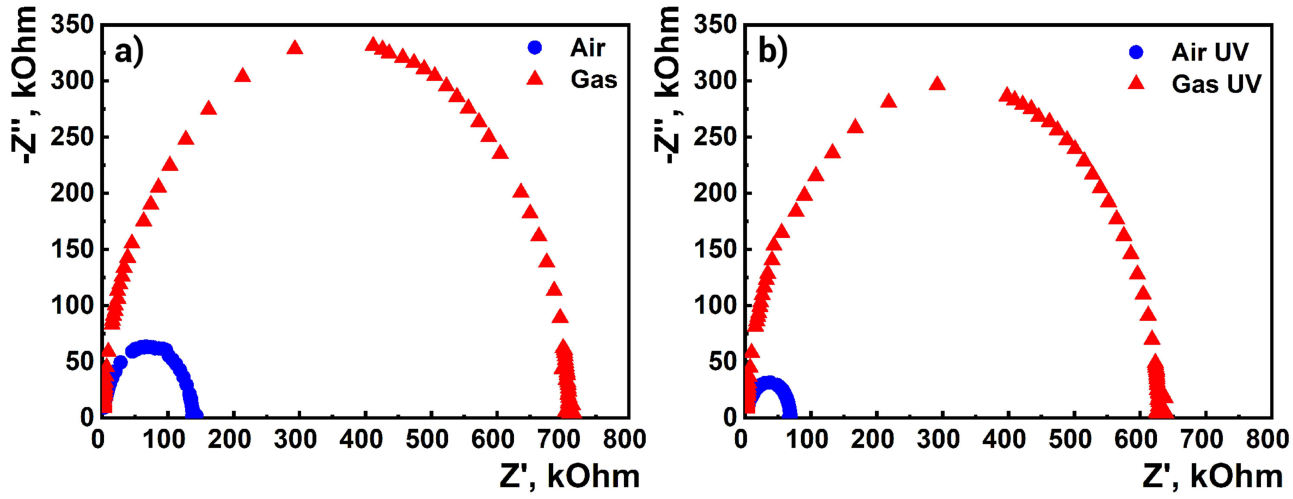

Figure 12 Transformation of the Nyquist semicircles of the sensor structure under exposure to HPV, measured at room temperature without (**a**) and under UV irradiation (**b**).

from the metal oxide conduction band, generating ionized oxygen species (O^{2-}, O^{-}, O_2^{-}) and establishing an electron depletion layer, which increases the material's electrical resistance. The resulting modulation of the electron depletion layer directly influences charge carrier density and potential barriers at grain boundaries, dictating the magnitude and dynamics of the sensor resistance response to subsequent exposure to target gases.[38] As can be seen from the data in Tables 1 and 2, exposure to HPV affects only the parameter *R*, which confirms the resistive nature of the sensor.

Figure 13 presents the calculations for the sensor sensitivity dependencies. The sensitivity of the ZnO/MWCNTs sensor was evaluated from the impedance characteristics as the ratio of the absolute values of the complex impedance (Z_{gas}/Z_{air}), measured under exposure to HPV and in air. These values closely matched the sensitivity calculated from the resistance ratio (R_{gas}/R_{air}), which confirmed the resistive nature of the sensor. The calculated sensitivity of the sensor is presented as a function of frequency (Figure 13a) and temperature (Figure 13b). The sensor shown a visible response to 100 ppm hydrogen peroxide vapor at room temperature, making this concentration optimal for impedance analysis. The

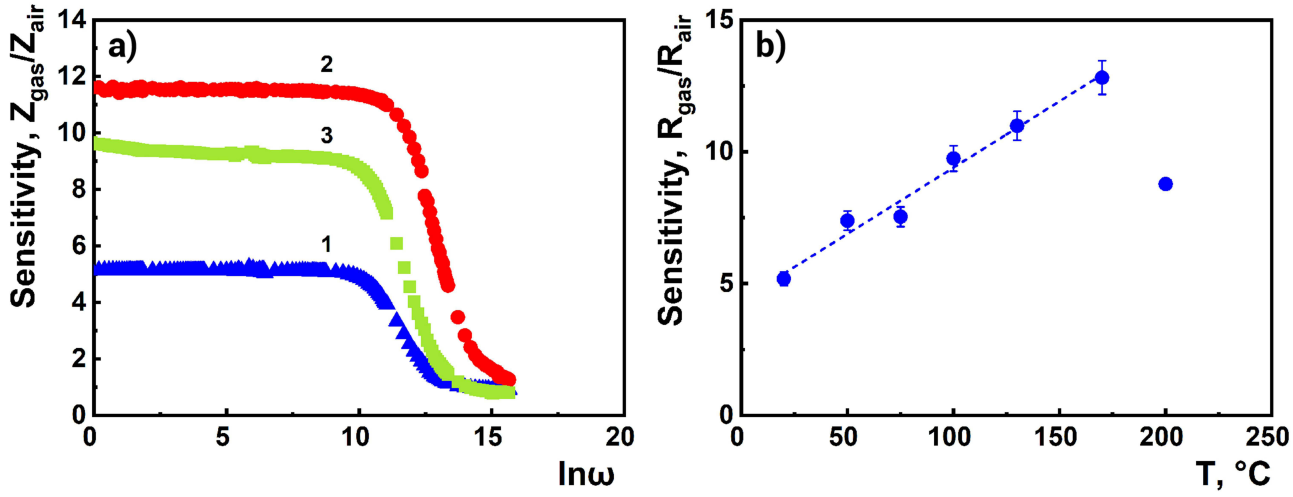

Figure 13 (**a**) Frequency dependence of the sensitivity of the ZnO/MWCNTs sensor, obtained from impedance measurements at 25 °C (1) and 175 °C (2) without UV illumination, and at 25 °C (3) under UV illumination. (**b**) Temperature dependence of the sensor on sensitivity, including the approximation curve (dashed line) and the error bars.

https://doi.org/10.2147/NSA.S577983

Table 3 Comparison of Key Sensing Parameters of HPV Sensors

Sensing Materials	Temperature, °C	Concentration, ppm	Response	References
Graphene aerogel	25	145	1.1	[39]
Multi-sensor chip	320	100	0.8	[40]
Cu(II) chelating chitosan	25	216	7	[41]
Copper-Pc and f-MWNTs	25	50	24.2%	[42]
Pt-SWCNTs	25	60.6	50.3%	[43]
SWCNTs with crystal violet	–	500	33%	[44]
ZnO/MWCNTs	20	100	5.2	This work
ZnO/MWCNTs	175	100	12.8	This work

sensitivity values at the temperatures of 25, 50, 75, 100, 125, 175, and 200 °C were 5.2, 7.4, 7.5, 9.7, 11.0, 12.8, and 8.8, respectively. A linear increase in sensitivity with rising temperature is observed up to 175 °C. The sensitivity remains nearly constant in the frequency range below approximately 10^3 Hz. Exposure to UV illumination results in a twofold increase in the sensor sensitivity at room temperature.

The sensing performance of the sensor for HPV detection is compared with other reported sensors in Table 3.

To evaluate the long-term stability of the sensor, stability tests were performed by monitoring the sensor response over an extended period (Figure 14a). In addition, the sensor was subjected to multiple bending cycles, and the response was measured after bending (Figure 14b). The results show only a very small drift in the sensor response, indicating good stability and mechanical reliability.

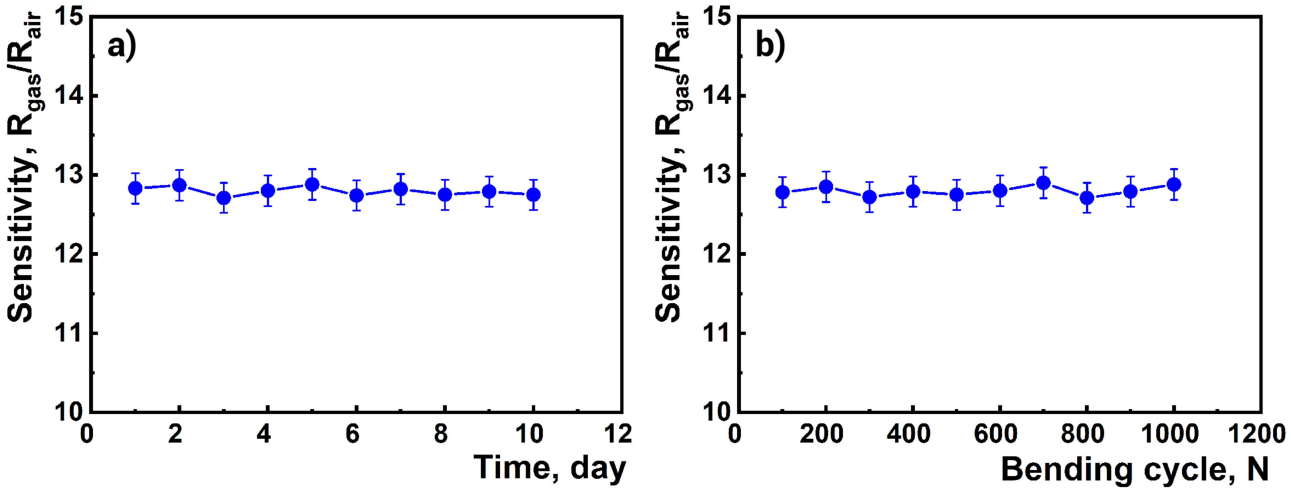

Figure 14 Long-term (**a**) and bending (**b**) stability testing results of the sensor at 175 °C, where the dashed lines represent the fitted curves and the error bars indicate the deviations.

Conclusion

The fabricated sensor for HPV detection was based on a ZnO film deposited by RF magnetron sputtering, onto which MWCNTs were deposited in the form of nanoscaled clusters. The SEM analysis revealed ZnO nanograins with an average size of approximately 50 nm, while the XPS and EDS results further verified the elemental composition and structural integrity of the material, respectively. The energy barrier height between the grains was approximately 0.134 eV. The frequency dependence of the complex impedance of the flexible ZnO/MWCNTs thin-film sensor was investigated. Measurements were performed in air and in an HPV atmosphere, both with and without UV exposure. The maximum sensitivity of 12.8 was obtained at an operating temperature of 175 °C. It was established that the flexible polyimide substrate with platinum interdigitated electrodes makes a significant contribution to the impedance of the sensor structure in the form of a parallel capacitance ($C_0 \approx 1.67 \times 10^{-11}$ F). This parasitic capacitance complicates the modeling of the capacitance associated with the gas-sensitive film. The presence of a single semicircle in the impedance characteristics may indicate an overlap of the contributions from processes occurring within the grain bulk and at the grain boundaries. To describe the behavior of the sensor structure, an equivalent electrical circuit consisting of a parallel CPE and a resistor was proposed. The Nyquist plots, which was calculated by this equivalent circuit shown good agreement with the experimentally obtained impedance characteristics. The sensitivity of the ZnO/MWCNTs sensor at room temperature increased by a factor of two in the presence of UV irradiation. The obtained results confirm the resistive nature of the sensor, in which the primary response to the target gas is manifested as a change in the resistance of the gas-sensitive film. Further studies will focus on investigating the sensitivity of the ZnO/MWCNTs sensor to low HPV concentrations, as well as on isolating the intrinsic capacitance of the gas-sensitive film to achieve a deeper understanding of the interaction mechanisms with the target gas and the processes responsible for sensor sensitivity.

Funding

The research was supported by the Higher Education and Science Committee of MESCS RA (Research Project № 24LCG-2J001).

Disclosure

The authors declare no competing financial interest.

References

1. Barsoukov E, Macdonald JR, eds.. *Impedance Spectroscopy: Theory, Experiment, and Applications*. 3rd ed. Hoboken (NJ): John Wiley & Sons; 2018.
2. Schipani F, Miller DR, Ponce MA, Aldao CM, Akbar SA, Morris PA. Electrical characterization of semiconductor oxide-based gas sensors using impedance spectroscopy: a review. *Rev Adv Sci Engine*. 2016;5(1):1–20. doi:10.1166/rase.2016.1109
3. Brett CMA. Electrochemical impedance spectroscopy in the characterisation and application of modified electrodes for electrochemical sensors and biosensors. *Molecules*. 2022;27(5):1497. doi:10.3390/molecules27051497
4. Randviir EP, Banks CE. A review of electrochemical impedance spectroscopy for bioanalytical sensors. *Anal Methods*. 2022;14(45):4602–4624. doi:10.1039/D2AY00970F
5. Rheaume JM, Pisano AP. A review of recent progress in sensing of gas concentration by impedance change. *Ionics*. 2011;17(2):99–108. doi:10.1007/s11581-010-0515-1
6. Dutta K. Potential of impedance spectroscopy towards quantified analysis of gas sensors: a tutorial. *IEEE Sens J*. 2021;21(20):22220–22231. doi:10.1109/JSEN.2021.3082475
7. Elseady AAE, Lee I, Zhuge Y, Ma X, Chow CWK, Gorjian N. Piezoresistivity and AC impedance spectroscopy of cement-based sensors: basic concepts, interpretation, and perspective. *Materials*. 2023;16(2):768. doi:10.3390/ma16020768
8. Szafraniak B, Kusior A, Radecka M, Zakrzewska K. Impedance spectroscopy in H_2 sensing with TiO_2/SnO_2 nanomaterials. *Metrol Meas Syst*. 2020;27(3):417–425. doi:10.24425/mms.2020.134588
9. Pandey S, Kumar D, Parkash O, Pandey L. Equivalent circuit models using CPE for impedance spectroscopy of electronic ceramics. *Integr Ferroelectr*. 2017;183(1):141–162. doi:10.1080/10584587.2017.1376984
10. Tomaev VV, Moshnikov VA, Miroshkin VP, Gar'kin LN, Zhivago AY. Impedance spectroscopy of metal-oxide nanocomposites. *Glass Phys Chem*. 2004;30(5):461–470. doi:10.1023/B:GPAC.0000045928.95952.ba
11. Shahnazaryan GE, Shahkhatuni GA, Aleksanyan MS, Simonyan ZG, Aroutiounian VM, Sayunts AG. Investigations of the impedance characteristics of a nanostructured ZnO⟨La⟩ sensor for hydrogen peroxide vapors. *J Contemp Phys*. 2022;57(3):254–262. doi:10.1134/S106833722203015X
12. Shahnazaryan G, Aleksanyan M, Sayunts A, Simonyan Z, Papovyan R, Shahkhatuni G. Study of a nanostructured co-doped SnO_2 sensor for hydrogen peroxide vapor detection using impedance spectroscopy. *ACS Omega*. 2025;10(14):14452–14465. doi:10.1021/acsomega.5c00917

13. Trujillo RM, Barraza DE, Zamora ML, Cattani-Scholz A, Madrid RE. Nanostructures in hydrogen peroxide sensing. *Sensors*. 2021;21(6):2204. doi:10.3390/s21062204
14. Giaretta JE, Duan H, Oveissi F, Farajikhah S, Dehghani F, Naficy S. Flexible sensors for hydrogen peroxide detection: a critical review. *ACS Appl Mater Interfaces*. 2022;14(18):20491–20505. doi:10.1021/acsami.1c24727
15. Vinay P, Peter K, Ponnambalam RS. Solid state sensors for hydrogen peroxide detection. *Biosensors*. 2021;11(1):9.
16. Hussein MA, Khan A, Alamry KA. A highly efficient electrochemical sensor containing polyaniline/cerium oxide nanocomposites for hydrogen peroxide detection. *RSC Adv*. 2022;12(49):31506–31517. doi:10.1039/D2RA05041B
17. Rahman MM, Adeosun WA, Asiri AM. Fabrication of selective and sensitive chemical sensor development based on flower-flake La2ZnO4 nanocomposite for effective non-enzymatic sensing of hydrogen peroxide by electrochemical method. *Microchem J*. 2020;159:105536. doi:10.1016/j.microc.2020.105536
18. Wang M, Jiang X, Liu J, Guo H, Liu C. Highly sensitive H2O2 sensor based on Co3O4 hollow sphere prepared via a template-free method. *Electrochimica Acta*. 2015;182:613–620. doi:10.1016/j.electacta.2015.08.116
19. Kuo -C-C, Lan W-J, Chen C-H. Redox preparation of mixed-valence cobalt manganese oxide nanostructured materials: highly efficient noble metal-free electrocatalysts for sensing hydrogen peroxide. *Nanoscale*. 2014;6(1):334–341. doi:10.1039/C3NR03791F
20. Kumar R, Al-Dossary O, Kumar G, Umar A. Zinc oxide nanostructures for NO_2 gas–sensor applications: a review. *Nanomaterials*. 2015;7:97–120.
21. Septiani NLW, Saputro AG, Kaneti YV, et al. Hollow zinc oxide microsphere–multiwalled carbon nanotube composites for selective detection of sulfur dioxide. *ACS Appl Nano Mater*. 2020;3(9):8982–8996. doi:10.1021/acsanm.0c01707
22. Pathak P, Park S, Cho HJ. A carbon nanotube–metal oxide hybrid material for visible-blind flexible UV-sensor. *Micromachines*. 2020;11(4):368. doi:10.3390/mi11040368
23. Chen X-M, Cai Z-X, Huang Z-Y, Oyama M, Jiang Y-Q, Chen C. Ultrafine palladium nanoparticles grown on graphene nanosheets for enhanced electrochemical sensing of hydrogen peroxide. *Electrochimica Acta*. 2013;97:398–403. doi:10.1016/j.electacta.2013.02.047
24. Pandeeswari R, Jeyaprakash BG. High sensing response of β-Ga2O3 thin film towards ammonia vapours: influencing factors at room temperature. *Sens Actuators B Chem*. 2014;195:206–214. doi:10.1016/j.snb.2014.01.025
25. Chen Q, Peng LM. Measurement accuracy of the diameter of a carbon nanotube from TEM images. *APS J*. 2002;65:155431.
26. Toloman D, Popa A, Stan M, et al. Visible-light-driven photocatalytic degradation of different organic pollutants using Cu doped ZnO-MWCNT nanocomposites. *J Alloys Compd*. 2021;866:159010. doi:10.1016/j.jallcom.2021.159010
27. Bobenko NG, Bolotov VV, Egorushkin VE, et al. Experimental and theoretical study of electronic structure of disordered MWCNTs. *Carbon*. 2019;153:40–51. doi:10.1016/j.carbon.2019.06.104
28. Vijayanath S, Janaki K, Gopal R, Ragupathi C, Rangasamy B, Alam MM. Fabrication of highly efficient and cost-effective dye-sensitized solar cells using ZnO/MWCNT nanocomposite as photoanode. *J Solid State Electrochem*. 2023;27(1):183–194. doi:10.1007/s10008-022-05312-w
29. Sumi S, Prabhakar Rao P, Koshy P. Impedance spectroscopic investigation on electrical conduction and relaxation in manganese substituted pyrochlore type semiconducting oxides. *Ceram Int*. 2015;41(4):5992–5998. doi:10.1016/j.ceramint.2015.01.038
30. Jiang T, Ye X, Tian Z, et al. Sensitivity studies and optimization of an impedance-based biosensor for point-of-care applications. *Biosens Bioelectron X*. 2024;18:100479.
31. Al-Hardan NH, Abdullah MJ, Abdul Aziz A. Sensing mechanism of hydrogen gas sensor based on RF-sputtered ZnO thin films. *Int J Hydrogen Energy*. 2010;35(9):4428–4434. doi:10.1016/j.ijhydene.2010.02.006
32. Shahrbabaki Z, Farajikhah S, Ghasemian MB, et al. A flexible and polymer-based chemiresistive CO_2 gas sensor at room temperature. *Adv Mater Technol*. 2023;8(10):2201510. doi:10.1002/admt.202201510
33. Imali DY, Perera ECJ, Kaumala MN, Dissanayake DP. Fabrication and characterization of a flexible and disposable impedance-type humidity sensor based on polyaniline (PAni). *RSC Adv*. 2023;13(10):6396–6411. doi:10.1039/D3RA00009E
34. da Silva GMG, Faia PM, Mendes SR, Araújo ES, da Silva GMG. A review of impedance spectroscopy technique: applications, modelling, and case study of relative humidity sensors development. *Appl Sci*. 2024;14(13):5754. doi:10.3390/app14135754
35. Adamchuck DV, Ksenevich VK, Gorbachuk NI, Shimanskij VI. Impedance spectroscopy of polycrystalline tin dioxide films. *Devices Meas Methods*. 2016;7(3):312–320.
36. Aleksanyan M, Sayunts A, Shahkhatuni G, Simonyan Z, Aroutiounian V, Khachatryan E. Detection of hydrogen peroxide vapor using flexible gas sensor based on SnO_2 nanoparticles decorated with multi-walled carbon nanotubes. *Adv Nat Sci*. 2023;14(2):025001.
37. Aleksanyan M, Sayunts A, Shahkhatuni G, Simonyan Z, Kasparyan H, Kopecký D. Room temperature detection of hydrogen peroxide vapor by Fe_2O_3:ZnO nanograins. *Nanomaterials*. 2022;13(1):120. doi:10.3390/nano13010120
38. Zhou M, Sun H, Chen S, et al. Chemosensors for H2O2 detection: principles, active materials, and applications. *Chemosensors*. 2025;13(2):54. doi:10.3390/chemosensors13020054
39. Kaur A, Kaur J, Singh RC. Graphene aerogel based room temperature chemiresistive detection of hydrogen peroxide: a key explosive ingredient. *Sensors Actuators A*. 2018;282:97–113. doi:10.1016/j.sna.2018.09.033
40. Steffen R, Benno S, Hanno G, Matthias VG, Patrick W, Michael JS. Multi-sensor chip for the investigation of different types of metal oxides for the detection of H2O2 in the ppm range. *Phys Status Solidi Appl Mater Sci*. 2013;210(5):898–904.
41. Tingting L, Huashan W, Mingxiu Z. Fabrication of a solid H2O2 vapor sensor using Cu(II) chelating chitosan as catalyst and PVA/NaNO2 as electrolyte. *J Mater Sci*. 2020;31:12561–12569.
42. Verma AL, Saxena S, Saini GSS, Gaur V, Jain VK. Hydrogen peroxide vapor sensor using metal-phthalocyanine functionalized carbon nanotubes. *Thin Solid Films*. 2011;519(22):8144–8148. doi:10.1016/j.tsf.2011.06.034
43. Lee D-J, Choi S-W, Byun YT. Room temperature monitoring of hydrogen peroxide vapor using platinum nanoparticles-decorated single-walled carbon nanotube networks. *Sens Actuators B*. 2018;256:744–750. doi:10.1016/j.snb.2017.10.001
44. Patel V, Saha D, Kruse P, Selvaganapathy PR. Reagent-free hydrogen peroxide sensing using carbon nanotube chemiresistors with electropolymerized crystal violet. *ACS Appl Nano Mater*. 2022;5(3):3957–3966. doi:10.1021/acsanm.1c04540